

Toward Absolute Molecular Numbers in DNA-PAINT

Johannes Stein,^{†,§} Florian Stehr,^{†,§} Patrick Schueler,[†] Philipp Blumhardt,[†] Florian Schueder,^{†,‡} Jonas Mücksch,[†] Ralf Jungmann,^{†,‡} and Petra Schwille^{*,†,‡}

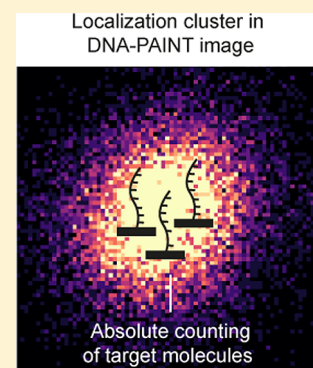
[†]Max Planck Institute of Biochemistry, 82152 Martinsried, Germany

[‡]Faculty of Physics, Ludwig Maximilian University, 80539 Munich, Germany

S Supporting Information

ABSTRACT: Single-molecule localization microscopy (SMLM) has revolutionized optical microscopy, extending resolution down to the level of individual molecules. However, the actual counting of molecules relies on preliminary knowledge of the blinking behavior of individual targets or on a calibration to a reference. In particular for biological applications, great care has to be taken because a plethora of factors influence the quality and applicability of calibration-dependent approaches to count targets in localization clusters particularly in SMLM data obtained from heterogeneous samples. Here, we present localization-based fluorescence correlation spectroscopy (lbFCS) as the first absolute molecular counting approach for DNA-points accumulation for imaging in nanoscale topography (PAINT) microscopy and, to our knowledge, for SMLM in general. We demonstrate that lbFCS overcomes the limitation of previous DNA-PAINT counting and allows the quantification of target molecules independent of the localization cluster density. In accordance with the promising results of our systematic proof-of-principle study on DNA origami structures as idealized targets, lbFCS could potentially also provide quantitative access to more challenging biological targets featuring heterogeneous cluster sizes in the future.

KEYWORDS: DNA-PAINT, super-resolution microscopy, single-molecule localization microscopy (SMLM), molecular counting, fluorescence correlation spectroscopy (FCS)



The advent of super-resolution (SR) microscopy has revolutionized life science research by providing visual access to specific biological structures at the nanoscale.^{1–4} The SR methods summarized as single-molecule localization microscopy (SMLM), such as stochastic optical reconstruction microscopy³ (STORM), photoactivated localization microscopy⁴ (PALM), and (DNA)-points accumulation for imaging in nanoscale topography^{5,6} (PAINT) circumvent the diffraction limit by acquiring image sequences of a “blinking” target structure by stochastically activating only a small subset of all fluorescent labels at a time. Thus, these methods enable localization of individual dye molecules in each camera frame and downstream rendering of SR images from the localizations obtained over all frames. Based on the fact that each targeted molecule contributes a certain number of localizations to the SR image, SMLM has been employed as a quantitative tool to count molecules for nearly a decade.^{7,8} Extensive efforts have been made in this direction particularly for the methods STORM/PALM^{7–22} mostly based on either (i) a priori knowledge of the blinking dynamics or the number of localizations per fluorescence marker (e.g., via supplementary experiments or theoretical modeling) or (ii) on an initial calibration directly within the sample by using isolated localization clusters originating from an assumed number of fluorescent molecules as a reference. Because a multitude of factors can influence the blinking dynamics locally in the sample,^{7,8} a calibration directly within the sample as in (ii) is

presumably the preferred option. Either way, however, when applying one of these counting approaches to localization clusters of unknown size, only relative counting results are obtained, determined by the a priori assumptions or by the assumed number of molecules within reference localization clusters.

In the special case of DNA-PAINT, an approach for molecular counting has been proposed, termed quantitative PAINT (qPAINT),²³ which exploits the programmable hybridization of single-stranded and fluorescently labeled DNA probes (“imagers”) to their complementary “docking strands” (DSs) fixed as labels to the target molecules. DNA-PAINT hence decouples the necessary “blinking” in SMLM from the photophysical properties of the fluorescent markers.^{7,24} However, when extracting DNA hybridization dynamics from DNA-PAINT data for molecular counting, one still has to consider several pitfalls both at the stage of data acquisition and post processing. On the acquisition side, this includes the choice of optimized illumination schemes for uniform spot detection efficiency²⁵ as well as minimizing photoinduced damage.²⁶ As typically high laser intensities are used in order to gain spatial resolution,²⁷ fluorescence bursts recorded during DNA-PAINT acquisition are usually limited

Received: August 28, 2019

Revised: September 16, 2019

Published: September 19, 2019

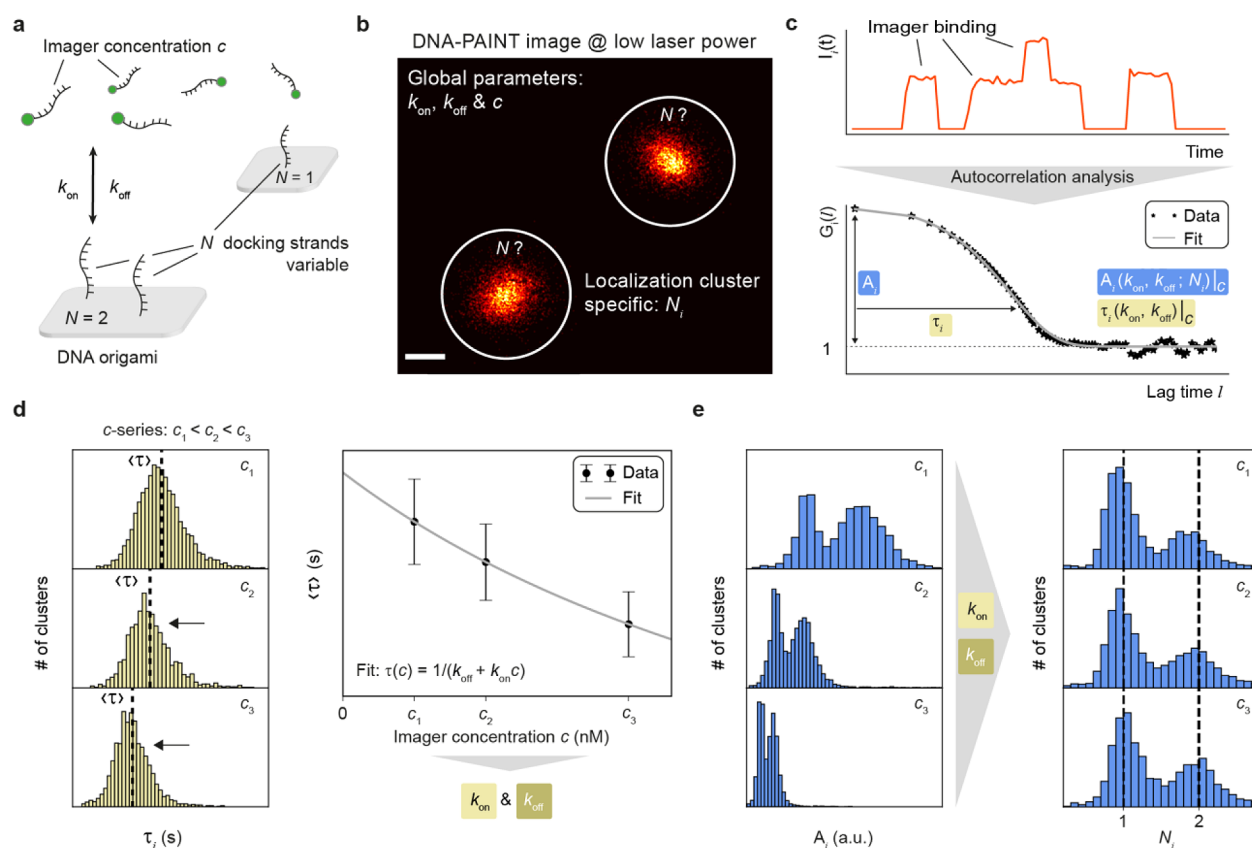


Figure 1. Principle of absolute molecular counting with lbFCS. (a) DNA-PAINT schematic for imaging DNA origami nanostructures exhibiting a variable number of docking strands (DSs) N (either $N = 1$ or $N = 2$). (b) DNA-PAINT image acquired at low laser power showing the two DNA origami from (a). The spatial resolution does not suffice to robustly distinguish the number of DSs N_i in the DNA-PAINT image. All localization clusters in an image are automatically detected as circular “picks” (white circles) for downstream DS counting analysis. (c) Top: for each pick, the intensity versus time trace containing the temporal information on imager binding and unbinding is analyzed by computing the autocorrelation function. Bottom: the computed autocorrelation curve of the intensity trace shows a characteristic monoexponential decay and is well described by the fit model with the two parameters amplitude A_i and characteristic decay time τ_i (eqs 1 and 2). (d) Extraction of DNA hybridization rates via imager concentration series. Left: histograms of τ_i distributions from all identified localization clusters (passing the filtering procedure as in Supplementary Figure 3) in the DNA-PAINT images of the same target, measured at three different imager concentrations c . The mean $\langle \tau \rangle$ (black dashed lines) decreases with c , as expected from eq 2. Right: Fitting eq 2 to $\langle \tau \rangle$ versus c yields k_{on} and k_{off} . (e) Left: distribution of A_i obtained from the same clusters as in the histograms in (d). Right: reformulating eq 1 and inserting (k_{on}, k_{off}, c) allows to convert each A_i to the number of DSs N_i in each cluster over all samples with peaks at $N = 1$ and $N = 2$ (black dashed lines). Scale bars: 50 nm in (b). Error bars correspond to standard deviation.

by photobleaching of the dye rather than the actual dissociation of the imager strands—an effect that can be accompanied by the photoinduced depletion of DSs during the course of a measurement.²⁶ Furthermore, qPAINT requires adjustment of the imager concentration to the expected density of DSs, limiting the applicability to biological samples, which might exhibit a heterogeneous distribution of DS densities.²³ On the postprocessing side, counting with qPAINT is also relative as it relies on the calibration to the hybridization kinetics of single DSs.²³

In this study, we introduce localization-based fluorescence correlation spectroscopy (lbFCS) as a quantitative tool for DNA-PAINT that, to our knowledge, for the first time allows absolute molecular ensemble counting in clusters of SMLM data. We first show that autocorrelation analysis of fluorescence fluctuations similar to classical FCS^{28,29} can be applied to localization clusters in DNA-PAINT images (i.e., the rendered localizations) of DNA origami structures³⁰ allowing the extraction of imager binding kinetics. Following previous work,³¹ our approach is based on imaging a sample at three different imager concentrations allowing extraction of the

hybridization rates via lbFCS at a precision of better than 5% and, most importantly, independent of the number of DSs per localization cluster. The DNA hybridization rates obtained over all localization clusters serve as calibration for lbFCS to subsequently count the number of DSs per cluster in each of the three samples. In order to minimize photoinduced damage and to obtain the true imager binding kinetics, we reduce the laser intensity for lbFCS measurements to a minimum while still allowing for efficient spot detection but at the cost of spatial resolution. In a benchmark study of lbFCS on DNA origami structures with a predesigned number of DSs, we additionally image each field of view (FOV) first at a low and then at a high laser power. This allows us to spatially resolve individual DSs as a visual ground truth for the lbFCS counting results over all localization clusters. Finally, we show that via lbFCS we can extend the restriction of qPAINT where the cluster densities (number of DSs) determine the applicable imager concentration. Over a wide range of cluster densities, we show that lbFCS counting results are in good agreement with the visual ground truth.

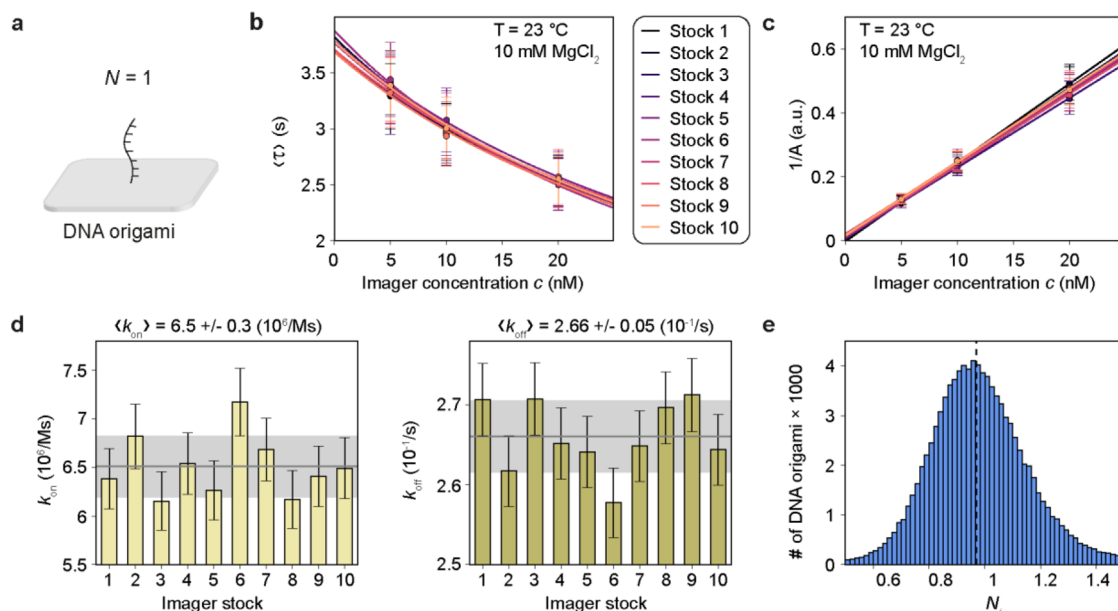


Figure 2. Experimental validation of lbFCS. (a) The 1DS structures with $N = 1$ for testing the lbFCS approach. (b) Repetition of 10 concentration series each with freshly prepared imager stocks (10×3 samples). $\langle \tau \rangle$ versus c fit for each concentration series demonstrating high reproducibility. (c) $1/A$ versus c fits show similar reproducibility. The fits passing through the origin yield that the concentration ratios were adjusted correctly. (d) Sets of k_{on} (left, light green) and k_{off} (right, dark green) extracted from the fits in (b) for each imager stock. Mean and standard deviation are given as gray line and light gray area, respectively. (e) Histogram of lbFCS counting results N over all 30 samples from the concentration series on 1DS structures. The black dashed line indicates the median at $N = 0.97 \pm 0.11$. Error bars correspond to standard deviation in the case of $\langle \tau \rangle$, k_{on} , and k_{off} and interquartile range in the case of $1/A$.

Results and Discussion. The Principle of lbFCS. As model targets for molecular counting with DNA-PAINT in this study we employed DNA origami,³⁰ a method allowing the precise and large scale production of artificial nanostructures from DNA as building material. In the context of DNA-PAINT, DNA origami have been extensively used for creating nanometer patterns of DSs as ideal benchmarking systems for the obtainable spatial resolution of the used microscope.^{6,32,33} In the following, we outline how to count the number of DSs on DNA origami structures in DNA-PAINT images with lbFCS (a detailed step-by-step description of all analysis steps can be found in [Supplementary Figure 1](#)). [Figure 1a](#) shows a DNA-PAINT schematic of two surface-immobilized DNA origami, one with two DSs ($N = 2$) and the other with a single DS ($N = 1$). Freely diffusing imagers bind to the DSs at association rate k_{on} and unbind at dissociation rate k_{off} , thereby generating the characteristic blinking required for downstream SMLM reconstruction. The concentration of imager strands is denoted as c . DNA-PAINT imaging was performed on a custom-built total internal reflection fluorescence (TIRF) microscope with a homogeneous (“flat-top”) intensity profile for optimized acquisition conditions²⁵ and temperature control (see [Supplementary Figure 2a](#) for a detailed setup sketch). A low laser power was selected to obtain imager dissociation rates unbiased by photobleaching ([Supplementary Figure 2b](#)) while still preserving the ability of robust spot detection. Albeit the reduction in laser power minimizes photoinduced damage during acquisition, it comes at the cost of reduced spatial resolution leaving clusters of localizations that do not allow counting of the number of DSs by eye ([Figure 1b](#)). However, lbFCS allows to count the number of DSs per structure solely based on the assumptions that (1) every target structure in the sample is subject to the same imager concentration c and (2) all individual DSs of the

target structures bind imager strands with equal hybridization rates given by k_{on} and k_{off} . This implies that the values k_{on} and k_{off} are determined for all structures in one sample (i.e., globally) by the designed sequence of the DS and the imager strand for a fixed set of environmental conditions (temperature, buffer, and so forth). Around each automatically detected cluster i in an image we define a circular region referred to as “pick” (white circles in [Figure 1b](#)) for which we plot the respective intensity versus time trace $I_i(t)$ containing the temporal information on imager binding and unbinding to the specific target structure ([Figure 1c](#), top). From these, we subsequently compute the autocorrelation curves $G_i(l)$ ([Figure 1c](#), bottom) which are well described by the monoexponential fit model previously derived for surface-integrated (SI)-FCS:^{31,34,35} $G_i(l) = A_i e^{l/\tau_i} + 1$. Here, l is defined as the autocorrelation lag time, A_i as the amplitude of the autocorrelation function at zero lag time $G_i(l = 0)$ and τ_i as the characteristic exponential decay constant. Following previous derivations,^{31,34,35} the model parameters are defined as

$$A_i(k_{\text{on}}, k_{\text{off}}; N_i)_c = \frac{1}{N_i} \frac{k_{\text{off}}}{k_{\text{on}} c} \quad (1)$$

and

$$\tau_i(k_{\text{on}}, k_{\text{off}})_c = \frac{1}{k_{\text{on}} c + k_{\text{off}}} \quad (2)$$

Referring to the previous assumptions of global hybridization rates and imager concentration, one can readily see that τ_i is only a function of the global rate constants k_{on} and k_{off} meaning that all picks in one sample of imager concentration c should yield the same value of τ_i within the uncertainty of the measurement. As a consequence the mean value $\langle \tau \rangle$ over all

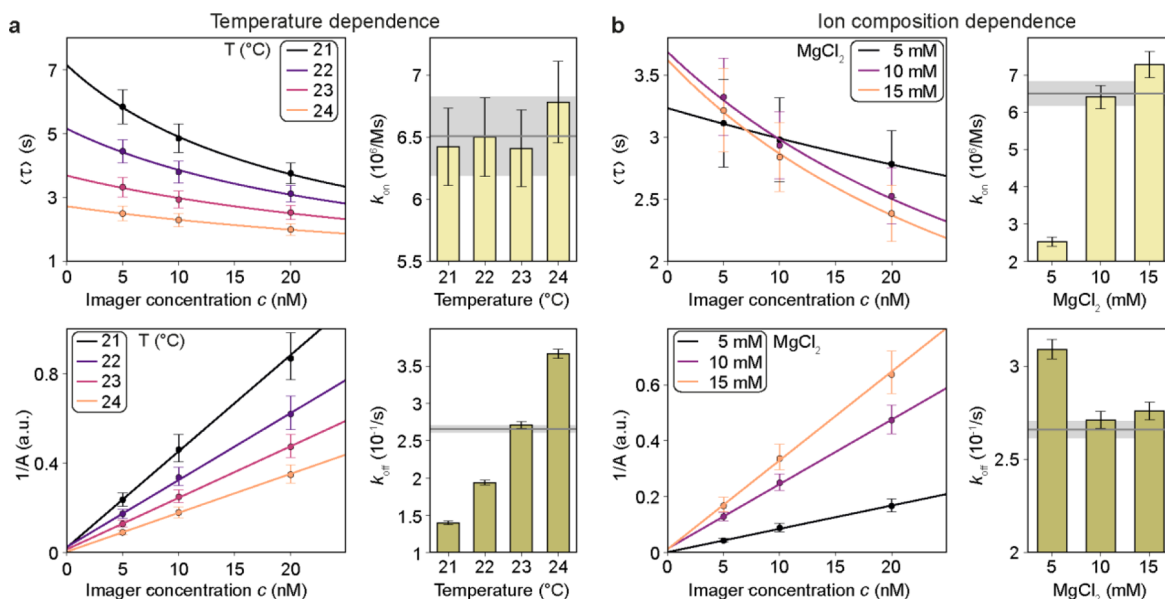


Figure 3. Temperature and ion composition affecting DNA hybridization rates. (a) lbFCS concentration series with 1DS samples at different temperatures, highlighting the temperature dependence of DNA hybridization rates (at fixed $[\text{MgCl}_2] = 10 \text{ mM}$). (b) lbFCS concentration series with 1DS samples at different MgCl_2 concentrations affecting the DNA hybridization rates (at fixed $T = 23 \text{ }^\circ\text{C}$). Gray lines and light gray shaded areas correspond to the mean and the standard deviation, respectively, of the hybridization rates at standard conditions ($T = 23 \text{ }^\circ\text{C}$ and $[\text{MgCl}_2] = 10 \text{ mM}$, see Figure 2d). Error bars correspond to standard deviation in the case of $\langle \tau \rangle$, k_{on} , and k_{off} and interquartile range in the case of $1/A$.

picks suffices for the extraction of the rate constants. The amplitude A_i in contrast is subject to the same global parameters but additionally depends on the number of DSs N_i in each pick. lbFCS makes use of these dependencies in order to extract both the hybridization rate constants k_{on} and k_{off} and the number of DSs N_i in each pick by the following procedure. First, we prepare and image three DNA origami samples (here exemplarily containing both $N = 1$ and $N = 2$ DNA origami structures) at three different imager concentrations ($c_1 < c_2 < c_3$) and automatically detect all clusters in the three resulting SR images (see Supplementary Figure 1). Next, we autocorrelate all intensity traces and remove clusters exhibiting nonrepetitive binding and/or binding dynamics deviating from a clear monoexponential behavior in a filtering step before further analysis (see Supplementary Figure 3). The left panel in Figure 1d shows the resulting τ_i histograms for all remaining clusters in each of the three images. As expected from eq 2, we observe a shift of the distributions toward lower values with increasing c corresponding to a decrease of the mean value $\langle \tau \rangle$. Following the aforementioned reasoning, the mean value $\langle \tau \rangle$ for each imager concentration c (Figure 1d, right panel) yields the global rate constants k_{on} and k_{off} by fitting eq 2. An analogous approach has been previously demonstrated using SI-FCS for the same system (i.e., DNA-PAINT on surface immobilized DNA origami) using an ensemble autocorrelation analysis of the raw intensity fluctuations integrated over larger arrays of camera pixels (originating from thousands of DNA origami), which allowed for the extraction of imager hybridization rates via a concentration series.³¹ Here, we show that this approach can be directly transferred to each localization cluster in a DNA-PAINT image of subdiffraction spatial resolution. This allows one to make further use of the amplitude A_i of each pick for molecular counting. According to eq 1, A_i depends on the number of DSs in each cluster resulting in a distribution exhibiting two peaks (for DNA origami either with $N = 1$ or

$N = 2$) in addition to the also concentration-dependent shift, as can be seen in the left panel of Figure 1e. Each A_i value can be converted into N_i by reformulating eq 1 to $N_i = \frac{1}{A_i} \frac{k_{off}}{k_{on}c}$ (Figure 1e, right) and inserting the now available rate constants k_{on} and k_{off} together with the respective imager concentration c of each measurement. Figure 1e, right, shows the distribution of the number of DSs present in each localization cluster (i.e., either one or two DSs).

Validation of lbFCS. In order to demonstrate the ability of lbFCS to extract DNA hybridization rates and to count DSs in DNA-PAINT images acquired at low laser power, we first explored the case of a DNA origami design exhibiting just a single DS ($N = 1$, referred to as “1DS”), as depicted in Figure 2a, because it is the only case of an implicit counting ground truth. In 10 repetitions of the same experiment over the course of 2 months, we prepared fresh imager stocks at 5, 10, and 20 nM for subsequent low laser power imaging on 1DS samples (10×3 samples, standard conditions: imaging buffer containing 10 mM MgCl_2 and temperature controlled at $23 \pm 0.1 \text{ }^\circ\text{C}$). lbFCS analysis of the localization clusters showed a good reproducibility with respect to the output parameters τ_i and A_i (Figure 2b,c). The mean (error bar, standard deviation) denoted as $\langle \tau \rangle$ of the τ_i distribution and the median (error bar, interquartile range) denoted as A of the A_i distribution (N and N_i) are shown whenever a statistical quantity of an ensemble is presented. The representation of $1/A$ in Figure 2c is chosen to verify the linear dependency on c (see eq 1). In addition, the plot serves as a control for whether the imager concentrations have been adjusted in the correct ratios when the fit of eq 1 intersects the y-axis at the origin. Figure 2d shows the scatter in k_{on} and k_{off} resulting from the 10 fits in Figure 2b. Over all measurements, we obtained the mean hybridization rates of $\langle k_{on} \rangle = (6.5 \pm 0.3) \times 10^6 \text{ M}^{-1} \text{ s}^{-1}$ and $\langle k_{off} \rangle = (2.66 \pm 0.05) \times 10^{-1} \text{ s}^{-1}$ with standard deviations below 5% and 2%, respectively, proving high reproducibility. We attribute this

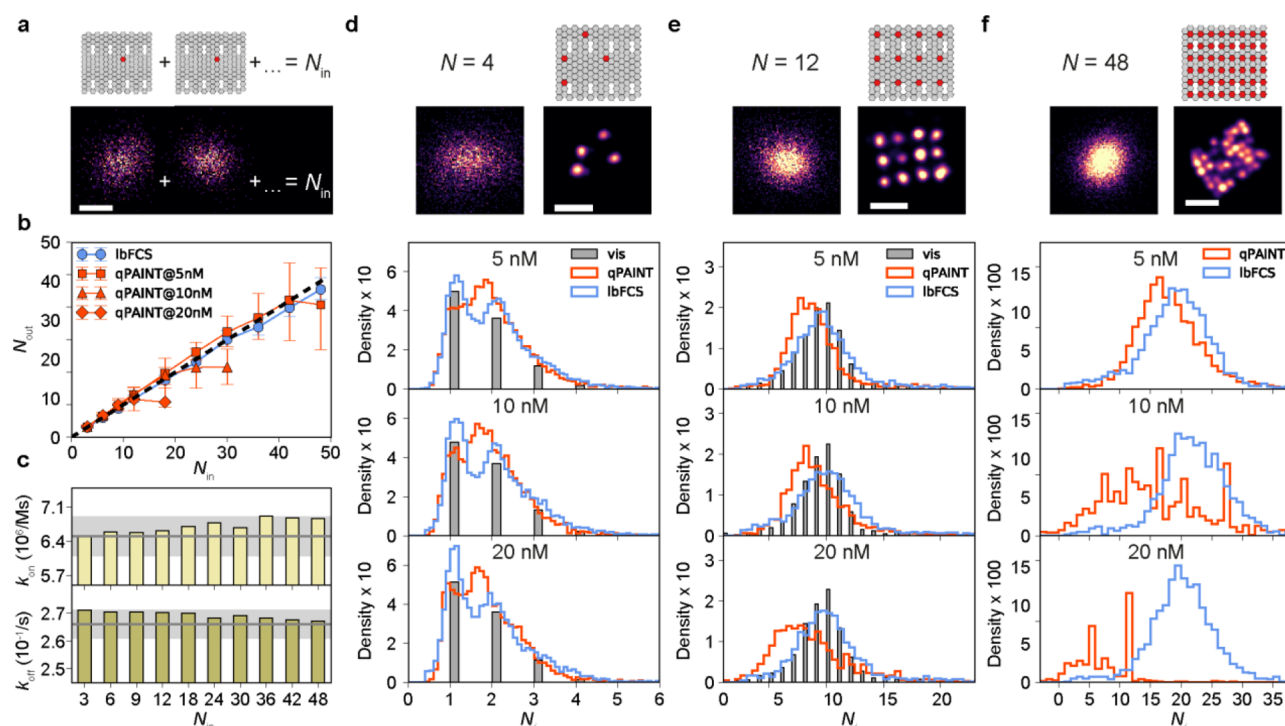


Figure 4. Counting of docking strands on DNA origami. (a) Binning of experimental 1DS localization clusters (taken from stock measurements 1–3, see Figure 2) for computationally increasing the number of DSs N_{in} as input for further testing of counting performance. (b) Median of the counting result N_{out} versus N_{in} comparing the counting results obtained via qPAINT at different imager concentrations (red) versus lbFCS (blue); sum over all imager concentrations displayed (see Supplementary Figure 9 for individual lbFCS and qPAINT results). The black dashed line displays a line through the origin of slope one as expected for ideal counting results (i.e., $N_{out} = N_{in}$). (c) lbFCS extracts correct hybridization rates within the measurement uncertainty independent of N_{in} (k_{on} and k_{off} means (gray lines) and STDs (light gray areas) from Figure 2d). (d) Top: DNA origami design with $N = 4$ DSs. Exemplary image of the same structure from the low laser power image (left) and the high laser power image for visual counting (right). Bottom: counting results for visual counting (gray), qPAINT (red) and lbFCS (blue). (e) Same as (d), but for $N = 12$ DSs DNA origami design. Intensity traces that do not exhibit dark times anymore (see Supplementary Figure 7) cannot be analyzed via qPAINT and are not shown in the histograms. Refer to Supplementary Table 1 for total numbers of analyzable clusters per histogram. (f) Same as (d,e) but for $N = 48$ DSs DNA origami design (no visual count histogram due to too tight DS spacing (10 nm) for robust spot detection). Scale bars: 40 nm in (a,d–f). Error bars in (b) correspond to interquartile range.

high precision to the fact that we are able to minimize the influence of unspecific binding to the surface (Supplementary Figure 4) by only analyzing detected clusters which, in addition, passed the filter criteria (see Supplementary Figure 3). Next, the values (k_{on} , k_{off}) for each stock were used to count the number of DSs in each of the three samples of the respective concentration series. Figure 2e shows the histogram of N_i over all 30 samples (>90% of all data points lie within the x -axis limits; >97 k localization clusters in total) with the median at $N = 0.97 \pm 0.11$, which is in good agreement with the initial design of the 1DS structures.

The counting ability of lbFCS is based on the assumption that k_{on} and k_{off} are global parameters which do not change during the course of the concentration series measurements. It is hence essential to precisely control the experimental conditions affecting DNA hybridization, such as temperature and buffer ion composition. In order to quantitatively assay these effects, we first repeated the concentration series on 1DS samples at 21–24 °C (1 °C increments, all at 10 mM $MgCl_2$), a temperature range which we observed due to the heating of the often enclosed sample space of commercial microscopes during imaging. As reported in many DNA hybridization studies before,^{32,36–38} Figure 3a shows that the dissociation rates change considerably (up to ~2.5-fold) over this temperature range, whereas the association rates do not change within the measurement error and show no observable

trend. We also varied the ion composition by changing the standard of 10 mM $MgCl_2$ by ± 5 mM (at 23 °C) and again used lbFCS to monitor the effects on both rates, such as the 3-fold increase in k_{on} between 5 and 10 mM (Figure 3b). However, as long as the rates are kept constant for all three concentration measurements, lbFCS yields the correct counting result of $N_i = 1$, independent of the actual temperature or ion composition (Supplementary Figure 5). Finally, the question of how precisely the absolute imager concentrations must be controlled needs to be addressed. In Supplementary Figure 6, we reanalyzed one of the stock measurement series at standard conditions as presented in Figure 1b–e by intentionally assuming higher or lower absolute imager concentrations while keeping the correct concentration ratios. The results clearly show that wrong absolute imager concentrations neither affect the absolute counting ability of lbFCS nor the resulting dissociation rate k_{off} as long as the correct concentration ratios are preserved (for which the 1/A fit provides control when crossing the origin). However, due to the product $k_{on}c$ in eq 2, assumed imager concentrations deviating from the “true” value by a factor of x will result in an obtained association rate multiplied by the inverse factor x^{-1} . To avoid this ambiguity in order to (relatively) compare obtained association rates we performed a control concentration series on 1DS origamis using the same

imager stock at standard conditions (see Figure 2b–e) for every measurement in this study.

Molecular Counting. As a next step, we tested the performance of lbFCS by arbitrarily grouping clusters of $N = 1$ obtained from earlier 1DS experiments (data taken from stock measurements 1–3; see Figure 2) into clusters of defined $N > 1$ ($\equiv N_{\text{in}}$) which is equivalent to the simple computational addition of their respective intensity versus time traces (see Figure 4a). This way, we created localization clusters of up to $N_{\text{in}} = 48$ for each imager concentration ($c = 5, 10$, and 20 nM) and analyzed them using lbFCS and qPAINT. It should be mentioned at this point that in contrast to lbFCS the counting of DSs with qPAINT needs a calibration²³ by the influx rate $k_{\text{on}}^{\text{qPAINT}} c$ obtained from clusters containing a single DS only (see Supplementary Figure 7 for the principle of the qPAINT approach). Supplementary Figure 8 displays the results as obtained by qPAINT analysis of the 1DS experiments of Figure 2b–e. The following results from molecular counting with qPAINT hence rely on a calibration association rate of $k_{\text{on}}^{\text{qPAINT}} = (7.7 \pm 0.2) \times 10^6 \text{ M}^{-1} \text{ s}^{-1}$. With respect to the error we would like to note that also $k_{\text{on}}^{\text{qPAINT}}$ is profiting from the filtering procedure introduced in Supplementary Figure 3, which in turn is based on the unique property of the autocorrelation analysis of lbFCS to identify and exclude clusters exhibiting dynamics that deviate from a clear monoexponential behavior.

Figure 4b displays the analysis results N_{out} versus N_{in} for both analysis methods (for lbFCS the sum over all three imager concentrations is displayed. See Supplementary Figure 9a–c for individual results at $c = 5, 10$, and 20 nM, respectively). As expected, lbFCS does not show any concentration dependence and yields the correct counting results ($N_{\text{out}} = N_{\text{in}}$, indicated by black dashed line) over the whole range of N_{in} . In contrast, qPAINT starts underestimating the correct number of DSs at a certain cluster size, an effect depending on the imager concentration (whereas for $c = 5$ nM qPAINT starts deviating from the linear relation at $N_{\text{in}} \sim 48$, for $c = 20$ nM the deviation already occurs at $N_{\text{in}} \sim 12$). As explained in Supplementary Figure 10, this is due to the increasing occurrence of simultaneous imager binding to multiple DSs within the same cluster. Because the qPAINT algorithm is based on the extraction of dark times from the intensity versus time trace of a cluster, its intrinsic limit given a certain imager concentration is determined by the maximum number of DSs per cluster N at which the corresponding intensity trace exhibits only few and, ultimately, no dark times at all anymore (in other words, the cluster is continuously fluorescing during data acquisition due to constant imager turnover). In accordance with this consideration, Figure 4b shows that the higher the imager concentration, the faster this limit determined by N is reached (see Supplementary Figure 9 for a detailed analysis of the number of unique dark times extracted per cluster for the last qPAINT data points for $c = 5, 10$, and 20 nM at $N = 48, 30$, and 18 , respectively). It should be discussed, however, that our DNA-PAINT data deviates from the type of data previously subjected to qPAINT analysis²³ in two aspects: (i) due to the low laser intensity, the bright times are an order of magnitude longer (i.e., not limited by fast photobleaching as in classical high-resolution DNA-PAINT) and (ii) the imager-DS sequence design employed in this study has a significantly higher $k_{\text{on}}^{\text{qPAINT}}$ (here $7.7 \times 10^6 \text{ M}^{-1} \text{ s}^{-1}$ versus previously²³ $1 \times 10^6 \text{ M}^{-1} \text{ s}^{-1}$). Hence, our probability of simultaneous binding events is

largely increased for a given N and imager concentration c (i.e., the limit of qPAINT is reached already for much smaller N compared to the previous study²³).

Having confirmed that lbFCS allows molecular counting over this wide range of DS densities independent of the imager concentration, we next validated the assumption that lbFCS can extract the correct DNA hybridization rates independent of N . Figure 4c displays that for all N_{in} we obtained the same hybridization rates within the measurement uncertainty verifying eq 2 and confirming that τ_i is indeed independent of the number of DSs per cluster.

In order to fully experimentally benchmark the counting performance of lbFCS, we designed DNA origami species with higher numbers of DSs ($N = 4, 12$, and 48). Like for the 1DS structures, we prepared three samples per DNA origami species at $c = 5, 10$, and 20 nM and measured each sample first at low laser power. Directly after each low power measurement, we imaged the same FOV at high laser power in order to obtain visual references at high resolution assignable to each of the localization clusters from the low power measurement. The top panel in Figure 4d depicts the $N = 4$ DNA origami design, an example DNA-PAINT image of a single structure acquired at low laser power (left) and the respective high power image exhibiting the four DSs in the designed pattern (right). We subsequently applied a spot detection algorithm to the high power image in order to automatically count the number of present DSs as a ground truth for the lbFCS and qPAINT results from the low laser power images. The efficiency by which individual staple strands are incorporated into each DNA origami during the folding process is limited and also position dependent,³⁹ that is, only very few structures feature all DSs from the initial design. The lower panel in Figure 4d shows the counting results of lbFCS (blue) and qPAINT (red) from the low power measurements as well as the visual counting results (gray) from the high power measurements for the three samples of $N = 4$ structures. Folding of this DNA origami design resulted in structures primarily exhibiting one or two DSs, which can be seen at the distinct peaks in all lbFCS distributions and which is furthermore in good agreement with the visual reference (refer to Supplementary Figure 11a for a comparison of the lbFCS/qPAINT performance with respect to individual integers from the visual inspection). Also qPAINT yields a distribution covering the lbFCS and visual results, even for the sample imaged at $c = 20$ nM (as expected from Figure 4b for the regime $N < 6$). In contrast, the qPAINT distribution does not feature clear and distinct peaks. Figure 4e illustrates the counting results for the measurement series on the $N = 12$ structures. Again lbFCS produces counting results which correlate well with the visual counting reference (see Supplementary Figure 11b for integer-wise comparison with visual inspection), both peaking at around $N \approx 10$ and both exhibiting the same distribution shape. However, for qPAINT we obtained a slightly left-shifted distribution even for the sample imaged at $c = 5$ nM, which further increased and broadened for the $c = 10$ and 20 nM samples. As expected from Figure 4b, intensity traces extracted from these samples started to lack enough unique dark times for qPAINT analysis (compare Supplementary Figures 7 and 9. The total number of analyzable clusters in each data set from Figure 4d–f are given in Supplementary Table 1). At last, we imaged the series of samples containing $N = 48$ structures (Figure 4f). As can be seen in the top panel, we were able to partially resolve the DSs tightly packed at a 10 nm spacing in

the DNA-PAINT images. However, the spatial resolution did not suffice to robustly run the spot detection algorithm earlier employed for the $N = 4$ and $N = 12$ origami for an unbiased visual ground truth. The DS incorporation efficiency leads to a broader spread in the actual number of DSs over all DNA origami structures with increasing N , which is in agreement with a broadening in the distribution of counted DSs by lbFCS compared to the previous DNA origami designs with less DSs. However, for all three imager concentrations lbFCS yielded the same counting results with a median of around $N \approx 25$. Although for the $c = 5$ nM sample the qPAINT results are in relatively good agreement with lbFCS, the distribution for the 10 nM sample is broadened and again shifted to the left due to lacking unique dark times extractable from the respective intensity versus time traces. As expected from Figure 4b, for $c = 20$ nM the DS density of the DNA origami design is already beyond the applicable limit of qPAINT since almost 75% of all clusters did not exhibit a single dark time anymore (see Supplementary Table 1).

Finally, we investigated whether even during the low laser power measurements the effect of photoinduced DS depletion via reactive oxygen species (ROS) generated upon excitation of dye molecules can be observed, as previously described by Blumhardt et al.²⁶ For the $N = 12$ structure, we repeated the concentration series with fresh samples this time measuring four times longer than a usual low power measurement without the use of an oxygen scavenging and triplet state quenching system (4×30 min). We then temporally segmented the total data set into four subsets and analyzed each subset individually via lbFCS. Supplementary Figure 12a depicts the resulting $\langle \tau \rangle$ versus c dependencies for all segments. We observed no significant difference between the time segments indicating that hybridization rates were unaffected and giving direct evidence that there was no bleaching of the imager solution (i.e., decreasing c) during the course of the 2 h measurement. Bearing this in mind, the clear change in $1/A$ versus c as shown in Supplementary Figure 12b is a direct consequence of the depletion of DSs leading to a decrease in N (compare eq 1). Supplementary Figure 12c shows the counting results over all segments normalized to the value of the first segment for every concentration. For an imager concentration of 20 nM, more than 20% of the DSs were depleted after 2 h of measurement. Furthermore, we observed an increase of the depletion rate with increasing imager concentration which is in agreement with previous results showing that the probability of photo-induced damage scales with the DS occupancy.²⁶ With respect to the results in Supplementary Figure 12b, this additionally explains why an offset in $1/A$ is becoming apparent for the later segments, as the $1/A$ values of different concentrations already originate from origamis of different N due to different depletion rates.

One of the proposed strategies to circumvent DS depletion is the use of oxygen scavenging systems such as pyranose oxidase, catalase, and glucose (POC) to directly remove ROS from the solution upon generation.²⁶ We repeated the same extended low power measurement series with POC and Trolox (a commonly used triplet state quencher) added to the imaging buffer. Subsequent lbFCS analysis revealed neither changes in $\langle \tau \rangle$ nor in $1/A$ over the four time segments (Supplementary Figure 12d,e). Hence, usage of oxygen scavenging systems allows one to virtually eliminate DS depletion during the low laser power measurements for lbFCS (Supplementary Figure 12e,f).

In conclusion, we presented lbFCS as an absolute counting approach for DNA-PAINT microscopy in a proof-of-principle study targeting DNA origami structures as ideal samples. On the basis of imaging a target of interest at several imager concentrations, we showed that lbFCS allows the extraction of imager hybridization rates at high precision from target clusters independent of the number of DSs within a cluster, which subsequently serves as calibration for counting of DS numbers within all clusters. We first confirmed the measurement principle on DNA origami exhibiting only a single DS and assayed the measurement uncertainty and the influence of experimental conditions such as temperature and buffer ion concentration. Next, we examined the performance of lbFCS to count the increasing number of DSs per cluster and compared the obtained results to the state-of-the-art DNA-PAINT counting approach qPAINT. We first increased the cluster size in a controlled way by grouping experimentally obtained clusters containing only a single DS into clusters of defined N . The obtained results show that lbFCS yields the correct counts over a range of more than 40 DSs for various imager concentrations in contrast to qPAINT. In addition, the extracted hybridization rates were unaffected by the number of DSs per cluster within the measurement uncertainty. Subsequent experimental benchmarking of lbFCS on DNA origami structures exhibiting multiple DSs yielded counts in good agreement with the visual ground truth obtained from high-resolution images from the respective FOVs. Finally, we could confirm previous results regarding the depletion of DSs in DNA-PAINT.²⁶ lbFCS is sensitive enough to detect slight changes in N due to depleted DSs and gave direct evidence that neither the hybridization rates nor the “effective” imager concentrations were affected by the employed low laser intensities during image acquisition. The usage of oxygen scavenging systems helped to virtually eliminate the depletion of DSs, underlining the applicability of our approach.

The work presented in this study was based on surface-immobilized DNA origami structures as model targets for DNA-PAINT microscopy. It should be highlighted that in this case all presented counting results here could also be obtained correctly via qPAINT when the imager concentration is adjusted according to the DS density. qPAINT could in principle also deal with samples containing heterogeneous cluster densities by imaging the sample at different imager concentrations. We particularly see the strength of lbFCS in future applications to DNA-PAINT data of biological samples, where it might be hard to identify enough single DSs for a robust calibration of the qPAINT influx rate. Additionally, local factors such as charge differences or steric hindrance effects introduced, for example, by the labeling linker to the target molecule, might lead to changes in the imager association rate limiting the applicability of the calibration rate obtained from DSs on DNA origami. While lbFCS could potentially solve these problems, the way toward cellular samples bears several difficulties that still remain to be tested. These include, among others, the effects of elevated background fluorescence, robust cluster identification and demands on achievable spatial resolution. We further would like to point out that lbFCS in its current state relies on the identification of spatially well-separated clusters and is hence not applicable to continuous structures (e.g., filaments).

Despite the focus on molecular counting presented here, the scope of lbFCS essentially exceeds the study of specific DNA–DNA interactions as in DNA-PAINT. We see promising

applications translating the high precision of lbFCS to study specific and reversible DNA–protein and protein–protein interactions with one of the species immobilized on a surface. In addition, lbFCS could also find application in structural in vitro studies to count subunits of immobilized multimeric complexes.

When targeting fixed cells, however, future work needs to address possible local changes in DNA hybridization rates, which might lead to large deviations between DSs and clusters. A next step in this direction will be combining lbFCS with Exchange-PAINT⁴⁰ in order to acquire the imager concentration series at the same FOV of a sample, potentially providing access to local changes in hybridization rates and allowing direct calibration with the cluster-specific rates for more robust counting. Finally, the same FOV would be imaged at high laser intensity for obtaining a DNA-PAINT image at highest spatial resolution. Complementing high-resolution DNA-PAINT images with an additional layer of robust quantitative information obtained via lbFCS has the potential to move the technology away from artificial or well-studied structures toward physiologically relevant targets and, ultimately, biological discovery.

■ ASSOCIATED CONTENT

■ Supporting Information

The Supporting Information is available free of charge on the ACS Publications website at DOI: 10.1021/acs.nanolett.9b03546.

Supplementary methods and figures (PDF)

■ AUTHOR INFORMATION

Corresponding Author

*E-mail: schwille@biochem.mpg.de.

ORCID

Johannes Stein: 0000-0002-1335-1120

Florian Schueder: 0000-0003-3412-5066

Jonas Mücksch: 0000-0002-1469-6956

Ralf Jungmann: 0000-0003-4607-3312

Petra Schwille: 0000-0002-6106-4847

Author Contributions

J.S., F.Stehr, R.J., and P.Schwille conceived the study. J.S. designed and performed the experiments, analyzed and interpreted the data, and wrote the manuscript. F.Stehr designed and performed the experiments, analyzed and interpreted data, and wrote the manuscript. F.Stehr wrote the code and J.S. edited code. P.Schueler folded DNA origami structures, performed experiments, and analyzed data. P.B., F.Schueder and J.M. performed initial experiments and interpreted the data. R.J. and P.Schwille supervised the study. All authors revised the manuscript and have given approval to the final version of the manuscript.

Author Contributions

§J.S. and F. Stehr contributed equally.

Funding

This work has been supported in part by the German Research Foundation through the Emmy Noether Program (DFG JU 2957/1-1 to R.J.), the SFB1032 (projects A11 and A09 to R.J. and P. Schwille), the European Research Council through an ERC Starting Grant (MolMap; Grant Agreement 680241 to R.J.) and the Max Planck Society (P.Schwille and R.J.).

Notes

The authors declare no competing financial interest.

■ ACKNOWLEDGMENTS

We thank Julian Bauer, Tamara Heermann, Henri Franquelim, Sigrid Bauer, and Katharina Nakel for experimental assistance and helpful discussions. J.S. and F. Stehr acknowledge support from Graduate School of Quantitative Bioscience Munich (QBM). P.B. and J.M. acknowledge support from the International Max Planck Research School for Molecular and Cellular Life Sciences (IMPRS-LS). All authors acknowledge support from the Center for Nano Science (CeNS).

■ ABBREVIATIONS

SMLM, single-molecule localization microscopy; (q)PAINT, (quantitative) points accumulation for imaging in nanoscale topography; DS, docking strand; FCS, fluorescence correlation spectroscopy; lbFCS, localization-based FCS; TIRF, total internal reflection fluorescence; SI-FCS, surface-integrated FCS; FOV, field of view; ROS, reactive oxygen species; POC, pyranose oxidase, catalase, and glucose

■ REFERENCES

- (1) Hell, S. W.; Wichmann, J. Breaking the diffraction resolution limit by stimulated emission: stimulated-emission-depletion fluorescence microscopy. *Opt. Lett.* **1994**, *19*, 780–782.
- (2) Hell, S. W.; et al. The 2015 super-resolution microscopy roadmap. *J. Phys. D: Appl. Phys.* **2015**, *48*, 443001.
- (3) Rust, M. J.; Bates, M.; Zhuang, X. Sub-diffraction-limit imaging by stochastic optical reconstruction microscopy (STORM). *Nat. Methods* **2006**, *3*, 793.
- (4) Betzig, E.; et al. Imaging Intracellular Fluorescent Proteins at Nanometer Resolution. *Science (Washington, DC, U. S.)* **2006**, *313*, 1642–1645.
- (5) Sharonov, A.; Hochstrasser, R. M. Wide-field subdiffraction imaging by accumulated binding of diffusing probes. *Proc. Natl. Acad. Sci. U. S. A.* **2006**, *103*, 18911–18916.
- (6) Schnitzbauer, J.; Strauss, M. T.; Schlichthaerle, T.; Schueder, F.; Jungmann, R. Super-resolution microscopy with DNA-PAINT. *Nat. Protoc.* **2017**, *12*, 1198.
- (7) Baddeley, D.; Bewersdorf, J. Biological Insight from Super-Resolution Microscopy: What We Can Learn from Localization-Based Images. *Annu. Rev. Biochem.* **2018**, *87*, 965–989.
- (8) Nicovich, P. R.; Owen, D. M.; Gaus, K. Turning single-molecule localization microscopy into a quantitative bioanalytical tool. *Nat. Protoc.* **2017**, *12*, 453.
- (9) Annibale, P.; Vanni, S.; Scarselli, M.; Rothlisberger, U.; Radenovic, A. Quantitative Photo Activated Localization Microscopy: Unraveling the Effects of Photoblinking. *PLoS One* **2011**, *6*, No. e22678.
- (10) Annibale, P.; Vanni, S.; Scarselli, M.; Rothlisberger, U.; Radenovic, A. Identification of clustering artifacts in photoactivated localization microscopy. *Nat. Methods* **2011**, *8*, 527.
- (11) Hummer, G.; Fricke, F.; Heilemann, M. Model-independent counting of molecules in single-molecule localization microscopy. *Mol. Biol. Cell* **2016**, *27*, 3637–3644.
- (12) Laplante, C.; Huang, F.; Tebbs, I. R.; Bewersdorf, J.; Pollard, T. D. Molecular organization of cytokinesis nodes and contractile rings by super-resolution fluorescence microscopy of live fission yeast. *Proc. Natl. Acad. Sci. U. S. A.* **2016**, *113*, E5876–LP-E5885.
- (13) Nino, D.; Rafiei, N.; Wang, Y.; Zilman, A.; Milstein, J. N. Molecular Counting with Localization Microscopy: A Bayesian Estimate Based on Fluorophore Statistics. *Biophys. J.* **2017**, *112*, 1777–1785.

- (14) Golfetto, O.; et al. A Platform To Enhance Quantitative Single Molecule Localization Microscopy. *J. Am. Chem. Soc.* **2018**, *140*, 12785–12797.
- (15) Coltharp, C.; Kessler, R. P.; Xiao, J. Accurate Construction of Photoactivated Localization Microscopy (PALM) Images for Quantitative Measurements. *PLoS One* **2012**, *7*, No. e51725.
- (16) Lee, S.-H.; Shin, J. Y.; Lee, A.; Bustamante, C. Counting single photoactivatable fluorescent molecules by photoactivated localization microscopy (PALM). *Proc. Natl. Acad. Sci. U. S. A.* **2012**, *109*, 17436–17441.
- (17) Nan, X.; et al. Single-molecule superresolution imaging allows quantitative analysis of RAF multimer formation and signaling. *Proc. Natl. Acad. Sci. U. S. A.* **2013**, *110*, 18519–18524.
- (18) Puchner, E. M.; Walter, J. M.; Kasper, R.; Huang, B.; Lim, W. A. Counting molecules in single organelles with superresolution microscopy allows tracking of the endosome maturation trajectory. *Proc. Natl. Acad. Sci. U. S. A.* **2013**, *110*, 16015–16020.
- (19) Ehmann, N.; et al. Quantitative super-resolution imaging of Bruchpilot distinguishes active zone states. *Nat. Commun.* **2014**, *5*, 4650.
- (20) Fricke, F.; Beaudouin, J.; Eils, R.; Heilemann, M. One, two or three? Probing the stoichiometry of membrane proteins by single-molecule localization microscopy. *Sci. Rep.* **2015**, *5*, 14072.
- (21) Ricci, M. A.; Manzo, C.; García-Parajo, M. F.; Lakadamyali, M.; Cosma, M. P. Chromatin Fibers Are Formed by Heterogeneous Groups of Nucleosomes In Vivo. *Cell* **2015**, *160*, 1145–1158.
- (22) Rollins, G. C.; Shin, J. Y.; Bustamante, C.; Pressé, S. Stochastic approach to the molecular counting problem in superresolution microscopy. *Proc. Natl. Acad. Sci. U. S. A.* **2015**, *112*, E110–LP-E118.
- (23) Jungmann, R.; et al. Quantitative super-resolution imaging with qPAINT. *Nat. Methods* **2016**, *13*, 439.
- (24) Nikić, I.; et al. Debugging Eukaryotic Genetic Code Expansion for Site-Specific Click-PAINT Super-Resolution Microscopy. *Angew. Chem., Int. Ed.* **2016**, *55*, 16172–16176.
- (25) Stehr, F.; Stein, J.; Schueder, F.; Schwille, P.; Jungmann, R. Flat-top TIRF illumination boosts DNA-PAINT imaging and quantification. *Nat. Commun.* **2019**, *10*, 1268.
- (26) Blumhardt, P. Photo-Induced Depletion of Binding Sites in DNA-PAINT Microscopy. *Molecules* **2018**, *23*, 3165.
- (27) Deschout, H.; et al. Precisely and accurately localizing single emitters in fluorescence microscopy. *Nat. Methods* **2014**, *11*, 253.
- (28) Magde, D.; Elson, E.; Webb, W. W. Thermodynamic Fluctuations in a Reacting System—Measurement by Fluorescence Correlation Spectroscopy. *Phys. Rev. Lett.* **1972**, *29*, 705–708.
- (29) Eigen, M.; Rigler, R. Sorting single molecules: application to diagnostics and evolutionary biotechnology. *Proc. Natl. Acad. Sci. U. S. A.* **1994**, *91*, 5740–5747.
- (30) Rothmund, P. W.; Folding, K. DNA to create nanoscale shapes and patterns. *Nature* **2006**, *440*, 297.
- (31) Mücksch, J.; et al. Quantifying Reversible Surface Binding via Surface-Integrated Fluorescence Correlation Spectroscopy. *Nano Lett.* **2018**, *18*, 3185–3192.
- (32) Jungmann, R.; et al. Single-Molecule Kinetics and Super-Resolution Microscopy by Fluorescence Imaging of Transient Binding on DNA Origami. *Nano Lett.* **2010**, *10*, 4756–4761.
- (33) Steinhauer, C.; Jungmann, R.; Sobey, T. L.; Simmel, F. C.; Tinnefeld, P. DNA Origami as a Nanoscopic Ruler for Super-Resolution Microscopy. *Angew. Chem., Int. Ed.* **2009**, *48*, 8870–8873.
- (34) Thompson, N. L.; Burghardt, T. P.; Axelrod, D. Measuring surface dynamics of biomolecules by total internal reflection fluorescence with photobleaching recovery or correlation spectroscopy. *Biophys. J.* **1981**, *33*, 435–454.
- (35) Starr, T. E.; Thompson, N. L. Total Internal Reflection with Fluorescence Correlation Spectroscopy: Combined Surface Reaction and Solution Diffusion. *Biophys. J.* **2001**, *80*, 1575–1584.
- (36) Howorka, S.; Movileanu, L.; Braha, O.; Bayley, H. Kinetics of duplex formation for individual DNA strands within a single protein nanopore. *Proc. Natl. Acad. Sci. U. S. A.* **2001**, *98*, 12996–13001.
- (37) Dupuis, N. F.; Holmstrom, E. D.; Nesbitt, D. J. Single-molecule kinetics reveal cation-promoted DNA duplex formation through ordering of single-stranded helices. *Biophys. J.* **2013**, *105*, 756–766.
- (38) Ouldrige, T. E.; Sulc, P.; Romano, F.; Doye, J. P. K.; Louis, A. A. DNA hybridization kinetics: Zippering, internal displacement and sequence dependence. *Nucleic Acids Res.* **2013**, *41*, 8886–8895.
- (39) Strauss, M. T.; Schueder, F.; Haas, D.; Nickels, P. C.; Jungmann, R. Quantifying absolute addressability in DNA origami with molecular resolution. *Nat. Commun.* **2018**, *9*, 1600.
- (40) Jungmann, R.; et al. Multiplexed 3D cellular super-resolution imaging with DNA-PAINT and Exchange-PAINT. *Nat. Methods* **2014**, *11*, 313.